INTERNATIONAL JOURNAL FOR NUMERICAL METHODS IN FLUIDS
Int. J. Numer. Meth. Fluids 2003; **41**:809–822 (DOI: 10.1002/fld.459)

Parallel finite element simulation of mooring forces on floating objects

S. Aliabadi*,†, J. Abedi and B. Zellars

Department of Engineering, Clark Atlanta University, 223 James P. Brawley Dr. S. W., Atlanta, GA 30314, U.S.A.

SUMMARY

The coupling between the equations governing the free-surface flows, the six degrees of freedom non-linear rigid body dynamics, the linear elasticity equations for mesh-moving and the cables has resulted in a fluid-structure interaction technology capable of simulating mooring forces on floating objects. The finite element solution strategy is based on a combination approach derived from fixed-mesh and moving-mesh techniques. Here, the free-surface flow simulations are based on the Navier–Stokes equations written for two incompressible fluids where the impact of one fluid on the other one is extremely small. An interface function with two distinct values is used to locate the position of the free-surface. The stabilized finite element formulations are written and integrated in an arbitrary Lagrangian–Eulerian domain. This allows us to handle the motion of the time dependent geometries. Forces and momentums exerted on the floating object by both water and hawsers are calculated and used to update the position of the floating object in time. In the mesh moving scheme, we assume that the computational domain is made of elastic materials. The linear elasticity equations are solved to obtain the displacements for each computational node. The non-linear rigid body dynamics equations are coupled with the governing equations of fluid flow and are solved simultaneously to update the position of the floating object. The numerical examples includes a 3D simulation of water waves impacting on a moored floating box and a model boat and simulation of floating object under water constrained with a cable. Copyright © 2003 John Wiley & Sons, Ltd.

KEY WORDS: free-surface flows; mooring forces; finite element method; fluid-structure interaction

1. INTRODUCTION

There are many marine applications involving free-surface flows interacting with moored floating platforms and vessels. The mooring forces are important design parameters and need

* Correspondence to: S. K. Aliabadi, Computation and Modelling Laboratory, Department of Engineering, Clark Atlanta University, 223 James P. Brawley Dr. S. W., Atlanta, Georgia 30314, U.S.A.
† E-mail: aliabadi@cau.edu

Contract/grant sponsor: Army High Performance Computing Research Center, Army Research Laboratory; contract/grant number: DAAD19-01-2-0014
Contract/grant sponsor: DoD HPCMP, PET, Mississippi State University; contract/grant number: GS04T01BFC0060

Received 21 November 2001
Revised 8 October 2002

to be estimated very accurately. Advanced high performance simulation tools can be used to predict the magnitude of the mooring forces and estimate the level of stress concentrations on locations where the mooring forces act.

Computer modelling of mooring forces is complex. The partial differential equations governing the conservation of the mass and momentum need to be coupled with the six degrees of freedom non-linear rigid body dynamic equations to account for the position of the floating objects. The tensional forces in cables will act as point forces on the objects. The magnitude and direction of these forces also need to be determined in an iterative scheme through coupling techniques with the other governing equations. In addition, the motions of the objects in the computational domain need to be addressed.

Generally, there are two distinct approaches in the numerical simulation of free-surface flows (excluding panel method [1]). Depending on the physical characteristics of the problem, either 'moving-mesh' or 'fixed-mesh' techniques are used. In the moving-mesh techniques, the motion of the free-surface is absorbed by moving the computational nodes located on the free-surface [2, 3]. Most of the moving-mesh techniques are based on either the space-time finite element formulations [4, 5] or the Arbitrary Lagrangian–Eulerian (ALE) [6, 7] formulations. In the applications where the deformation of the free-surface is large, the moving-mesh techniques usually result in element distortions. As the element distortions grow and become unacceptable, the generation of a new mesh and the projection of the solution from the old mesh to the new one is essential [8]. In complex 3D applications, this procedure is extremely difficult and time consuming. In such cases, computations using fixed-mesh techniques are more desirable.

The most common fixed-mesh techniques are based on the VOF [9], the level-set [10, 11] and recently developed interface-sharpening/global mass conservation (IS-GMC) methods [12, 13]. In these methods, the Navier–Stokes equations are solved over a non-moving mesh. A scalar function (or colour function) as a marker identifies the location of the free-surface. This function is transported throughout the computational domain with a transient advection equation.

Our free-surface flow simulation techniques over fixed-meshes are based on the IS-GMC and advanced parallel computational technologies we have developed in the past several years [14, 15]. These computational technologies are very user friendly and have been applied to many applications including sloshing in tanker-trucks [2], waves interacting with marine vessels in motion [14, 15], and flow in open channels [12]. In the recent benchmark, we carried out computations using a totally unstructured mesh with more than one billion tetrahedral elements [15]. The sustained computational speed was measured at 115 Gigaflops on the Cray T3E-1200 with 1024 processors. The total time spent in inter-processor communication was between 1% and 2% of the total wall-clock time for the overall computation. This free-surface flow solver can produce solutions, which are highly accurate [2, 12, 13, 15].

In this article, we describe a new finite element method for simulation of mooring forces on floating objects. This finite element method combines the moving-mesh and fixed-mesh simulations techniques. Here, the physical motion of the floating objects will be handed using advanced mesh-moving schemes while the interface between the two fluids will be tracked by the interface function. This combination approach is a very effective simulation strategy to solve problems with relatively 'mild' physical motions and 'severe' deformation of the interface between the two fluids. This finite element method is based on the implementation of our IS-GMC free-surface flow solver in an Arbitrary Lagrangian–Eulerian (ALE) moving-mesh frame.

The mooring forces are simulated using both linear and non-linear mathematical models. In the linear model, we assume that the cables act as linear springs subjected to tensional forces (no resistance to the compression force). In the non-linear model, we use the transient, non-linear finite element formulation derived from the principal of virtual work. The mooring forces act as concentrated forces on floating objects and are constrains in the six degrees of freedom non-linear rigid body dynamic equations.

The governing equations and the finite element formulations are described in Section 2. The global mass conservation algorithm is described in Section 3. The iterative solution strategy is discussed in Section 4. The numerical example and results are provided in Section 5 following the concluding remarks in Section 6.

2. GOVERNING EQUATIONS AND FINITE ELEMENT FORMULATIONS

We consider the governing equations for two interacting fluids in the spatial domain Ω and its boundary Γ. Here we assume that the spatial domain and its boundary are both functions of time, t. The two fluids are incompressible (e.g. air–water) and separated with an interface. Along the interface, the traction force is continuous (surface tension is negligible). The governing equations of two fluids are the Navier–Stokes equations written in an Arbitrary Lagrangian–Eulerian (ALE) domain. These equations are:

$$\rho\left[\left.\frac{\partial \mathbf{u}}{\partial t}\right|_{\xi}+(\mathbf{u}-\mathbf{u}_{\text{mesh}})\cdot\nabla\mathbf{u}-\mathbf{g}\right]-\nabla\cdot\boldsymbol{\sigma}=0 \tag{1}$$

$$\nabla\cdot\mathbf{u}=0 \tag{2}$$

where

$$\boldsymbol{\sigma}=-\mathrm{p}\mathbf{I}+2\mu\boldsymbol{\varepsilon}(\mathbf{u}),\quad \boldsymbol{\varepsilon}=\frac{1}{2}(\nabla\mathbf{u}+\nabla\mathbf{u}^{\mathrm{T}}) \tag{3}$$

Here $\mathbf{u}$, $\mathbf{u}_{\text{mesh}}$, p, ρ, $\mathbf{g}$, and μ are the fluid velocity, mesh velocity, pressure, density, gravitational force, and dynamic viscosity, respectively. The strain tensor is denoted by $\boldsymbol{\varepsilon}$ and $\mathbf{I}$ represents the identity tensor. Equations (1) and (2) are completed by an appropriate set of boundary and initial conditions. The stabilized finite element formulations for Equations (1) and (2) are written as

$$\begin{aligned}
&\int_{\Omega}\mathbf{w}^{\mathrm{h}}\cdot\rho\left[\frac{\partial\mathbf{u}^{\mathrm{h}}}{\partial t}+(\mathbf{u}^{\mathrm{h}}-\mathbf{u}^{\mathrm{h}}_{\text{mesh}})\cdot\nabla\mathbf{u}^{\mathrm{h}}-\mathbf{g}\right]\mathrm{d}\Omega+\int_{\Omega}\boldsymbol{\varepsilon}(\mathbf{w}^{\mathrm{h}}):\boldsymbol{\sigma}(p^{\mathrm{h}},\mathbf{u}^{\mathrm{h}})\,\mathrm{d}\Omega\\
&\quad+\int_{\Omega}q^{\mathrm{h}}_{\mathrm{p}}\nabla\cdot\mathbf{u}^{\mathrm{h}}\,\mathrm{d}\Omega+\sum_{e=1}^{ne}\int_{\Omega^e}\frac{\tau_m}{\rho}[\rho(\mathbf{u}^{\mathrm{h}}-\mathbf{u}^{\mathrm{h}}_{\text{mesh}})\cdot\nabla\mathbf{w}^{\mathrm{h}}-\nabla\cdot\boldsymbol{\sigma}(q^{\mathrm{h}}_{\mathrm{p}},\mathbf{w}^{\mathrm{h}})]\\
&\quad\cdot\left[\rho\left[\frac{\partial\mathbf{u}^{\mathrm{h}}}{\partial t}+(\mathbf{u}^{\mathrm{h}}-\mathbf{u}^{\mathrm{h}}_{\text{mesh}})\cdot\nabla\mathbf{u}^{\mathrm{h}}-\mathbf{g}\right]-\nabla\cdot\boldsymbol{\sigma}(p^{\mathrm{h}},\mathbf{u}^{\mathrm{h}})\right]\mathrm{d}\Omega\\
&\quad+\sum_{e=1}^{ne}\int_{\Omega^e}\tau_{\mathrm{c}}\nabla\cdot\mathbf{w}^{\mathrm{h}}\rho\nabla\cdot\mathbf{u}^{\mathrm{h}}\,\mathrm{d}\Omega=\int_{\Gamma_{h_u}}\mathbf{w}^{\mathrm{h}}\cdot\mathbf{h}\,\mathrm{d}\Gamma
\end{aligned} \tag{4}$$

Here, $\mathbf{w}$ and q are linear test functions for the velocity and pressure, respectively. In this formulation, the first three integrals together with the right hand side term are the Galerkin finite element formulation. The first element-level integral includes the stabilizations [2]. The second element-level integral is the least-square stabilization of the continuity equation, which enhanced the robustness of the finite element formulation at high Reynolds numbers. The details of the stabilization techniques and the definitions of the coefficients τ_m and τ_c, can be found in References [2, 5, 12, 16, 17].

The interface function, ϕ, has two distinct values (0,1) and is used to differentiate between the two fluids. A transient advection equation transports this function throughout the computational domain with the fluid velocity as

$$\left.\frac{\partial \phi}{\partial t}\right|_{\xi} + (\mathbf{u} - \mathbf{u}_{\text{mesh}}) \cdot \nabla \phi = 0 \tag{5}$$

Using ϕ, the density and viscosity can be calculated as

$$\rho = \phi \rho_A + (1 - \phi)\rho_B, \quad \mu = \phi \mu_A + (1 - \phi)\mu_B \tag{6}$$

where the subscripts A and B denote the fluid A and fluid B. The artificial diffusion finite element formulation for Equation (5) leads to:

$$\int_{\Omega} \psi^{\text{h}} \left[\frac{\partial \phi^{\text{h}}}{\partial t} + (\mathbf{u}^{\text{h}} - \mathbf{u}^{\text{h}}_{\text{mesh}}) \cdot \nabla \phi^{\text{h}} \right] \mathrm{d}\Omega + \sum_{e=1}^{ne} \int_{\Omega^e} \tau_i \nabla \psi^{\text{h}} \cdot \nabla \phi^{\text{h}} \, \mathrm{d}\Omega = 0 \tag{7}$$

where ψ is a test function for the interface function. Here the first integral is the Galerkin finite element formulation and the second integral is the artificial diffusion stabilization. The artificial diffusion stabilization technique is used for over stabilization [2, 12]. This feature allows us to enforce the conservation of mass not only locally, but also globally. In the IS-GMS, the sharpness of the interface function is recovered after each non-linear iteration [12, 13, 15]. The details are discussed in Section 3.

The finite element formulations described in Equations (4) and (7) are solved sequentially. First, Equation (7) is solved to obtain the location of the interface. Using Equation (6), the density and viscosity of 'mixed-fluid' is computed and used in Equation (4) to obtain the pressure and velocity vector.

There is no limit on the number of cables, which can be attached to the floating objects. For non-linear cables, the governing equations are:

$$\rho_c \left(\frac{\partial^2 \mathbf{x}}{\partial t^2} - \mathbf{g} \right) = \nabla \cdot \mathbf{T} \tag{8}$$

$$\mathbf{x}|_{t=0} = \mathbf{X}, \quad \left.\frac{\partial \mathbf{x}}{\partial t}\right|_{t=0} = 0 \tag{9}$$

where $\mathbf{x}$ is the position vector, $\mathbf{X}$ is the initial position, ρ_c is the cable density, and $\mathbf{T}$ is the Cauchy stress tensor. Locally, the Green strain tenor has only one component, which can be defined as

$$\mathbf{E}_{11} = \frac{1}{2} \left(\left\| \frac{\partial \mathbf{x}}{\partial s} \right\|^2 - \left\| \frac{\partial \mathbf{X}}{\partial s} \right\|^2 \right) \tag{10}$$

where s is a tangent vector in the original configuration. The Cauchy stress tensor, $\mathbf{T}$, and the second Piola–Kirchoff stress tensor, $\mathbf{S}$, are related through geometry deformation. Under the assumption of small strain, but large geometry displacements, the only component of $\mathbf{S}$ in the s direction is defined as

$$\mathbf{S}_{11} = E_c \mathbf{E}_{11} \tag{11}$$

Here E_c is the Young's modulus of elasticity of the cable. The finite element formulation for Equation (8) is derived from the principle of virtual work [19] leading to

$$\rho_c \int_{\Gamma_0} \mathbf{H}^h \cdot \left(\frac{\partial^2 \mathbf{x}^h}{\partial t^2} + \boldsymbol{\theta} \frac{\partial \mathbf{x}^h}{\partial t} - \mathbf{g} \right) \mathrm{d}\Gamma + \frac{1}{2} E_c \int_{\Gamma_0} \left(\left\| \frac{\partial \mathbf{x}}{\partial s} \right\|^2 - \left\| \frac{\partial \mathbf{X}}{\partial s} \right\|^2 \right) \frac{\partial \mathbf{H}}{\partial s} \cdot \frac{\partial \mathbf{x}}{\partial s} \mathrm{d}\Gamma = 0 \tag{12}$$

where $\mathbf{H}$ is the test function for cable displacements. Here we assume that the fluid does not affect the cable motion directly. Instead, a numerical damping, $\boldsymbol{\theta}$, is introduced to dampen the oscillations in time. In this formulation, all the integrations are carried out in the original domain rather than current deformed domain.

For the linear model, we have:

$$\mathbf{S}_{11} = E_c \frac{\langle L_f - L_i \rangle}{L_i} \mathbf{e} \quad \langle L_f - L_i \rangle = \begin{cases} L_f - L_i & \text{if } L_f > L_i \\ 0 & \text{if } L_f \leqslant L_i \end{cases} \tag{13}$$

Here, L_f and L_i are the final and initial length of the cable, respectively.

The motions of the floating objects are handled using automatic mesh moving scheme. In this mesh-moving scheme, the mesh connectivity does not change as the nodes are moved to the new locations. Here, we assume that the computational domain is made of elastic material [8]. We solve linear elasticity equations to obtain the displacements for every computational node. These equations are:

$$\boldsymbol{\nabla} \cdot [\lambda_1 (\boldsymbol{\nabla} \cdot \mathbf{d}) \mathbf{I} + 2\lambda_2 \boldsymbol{\nabla} \boldsymbol{\kappa}(\mathbf{d})] = \mathbf{0}, \quad \boldsymbol{\kappa} = \frac{1}{2} (\boldsymbol{\nabla} \mathbf{d} + \boldsymbol{\nabla} \mathbf{d}^T) \tag{14}$$

where $\mathbf{d}$ is the displacement, $\boldsymbol{\kappa}$ is the strain tensor, and λ_1 and λ_2 are the linear elasticity coefficients. The finite element formulation for these equations is the Galerkin formulation written as

$$\int_\Omega \boldsymbol{\kappa}(\pi^h) : [\lambda_1 (\boldsymbol{\nabla} \cdot \mathbf{d}^h) \mathbf{I} + 2\lambda_2 \boldsymbol{\nabla} \boldsymbol{\kappa}(\mathbf{d}^h)] \, \mathrm{d}\Omega = 0 \tag{15}$$

where π is the test function for the displacements. In our computations, the computational cost associated with solving Equation (15) is accounted for 16% of the overall computational cost.

The six degrees of freedom non-linear rigid body dynamics are solved to locate the new position and orientation of the floating objects. Here we consider two co-ordinate systems, one attached to the computational domain, X, and the other attached to the floating object, Y. The rotation matrix, $\mathbf{Q}$, transfers components of any arbitrary vector from the X co-ordinate system to the Y co-ordinate system. The non-linear rigid body dynamic equations for the

center of the gravity of the object are:

$$\mathbf{F}_X - m\mathbf{g}_X = m\mathbf{a}_X \tag{16}$$

$$\mathbf{M}_X = [\mathbf{Q}^{\mathrm{T}}\mathbf{J}_Y\mathbf{Q}]\boldsymbol{\alpha}_X \tag{17}$$

where $\mathbf{F}_X$ and $\mathbf{M}_Y$ are the total force and angular momentum exerted on the center of gravity of the object by fluids, respectively. The linear and angular accelerations are $\mathbf{a}_X$ and $\boldsymbol{\alpha}_X$. The mass of the object is m and its moment of inertia is $\mathbf{J}_Y$. Here the subscribed X and Y denotes the co-ordinate system where components of the vectors and matrices are evaluated.

3. INTERFACE-SHARPENING/GLOBAL MASS CONSERVATION (IS-GMC)

The finite element formulation in Equation (7) introduces numerical diffusion for the interface function ϕ. To recover the sharpness of the interface function, after each iteration, ϕ is replaced by ϕ_{new} as follows:

$$\phi_{\text{new}} = \begin{cases} \beta\left(\dfrac{\phi}{\beta}\right)^{\alpha} & 0 \leqslant \phi \leqslant \beta \\ 1 - (1-\beta)\left(\dfrac{1-\phi}{1-\beta}\right)^{\alpha} & \beta \leqslant \phi \leqslant 1 \end{cases} \tag{18}$$

where $\boldsymbol{\alpha}$ is a sharpening parameter, and $0 \leqslant \beta \leqslant 1$ is a point satisfying the global conservation of mass for each fluid.

To determine β, we satisfy the mass conservation at a given time t for ϕ_{new}. Therefore:

$$\rho_A \int_\Omega \phi_{\text{new}}\, \mathrm{d}\Omega = m_A + \rho_A \int_t \int_\Gamma \phi \mathbf{u}\cdot\mathbf{n}\, \mathrm{d}\Gamma\, \mathrm{d}t \tag{19}$$

$$\rho_B \int_\Omega (1-\phi_{\text{new}})\, \mathrm{d}\Omega = m_B + \rho_B \int_t \int_\Gamma (1-\phi)\mathbf{u}\cdot\mathbf{n}\, \mathrm{d}\Gamma\, \mathrm{d}t \tag{20}$$

where m_A and m_B are the initial mass of Fluid A and Fluid B, respectively. Note that we only need to satisfy either Equation (19) or (20). Combining Equations (18) and (19) and assuming that the parameter $\boldsymbol{\alpha}$ is given and constant, we obtain:

$$M\beta^{(1-\alpha)} + N(1-\beta)^{(1-\alpha)} = R \tag{21}$$

where M, N, and R are all functions of β. This non-linear equation is solved using a Newton–Raphson algorithm. Typically, with the initial guess of 0.5, the algorithm converges in three iterations. In numerical experiment, the optimal $\boldsymbol{\alpha}$ is to be found between 1.2 and 1.5 [12, 13, 15].

4. ITERATIVE SOLUTION STRATEGY

After linearization using the Newton–Raphson algorithm, we need to solve a series of first order linear differential equation systems. These systems are also solved iteratively using the

GMRES update algorithm [16, 18, 20]. For very large systems of equations, we use a matrix-free iteration strategy [16, 18]. This element-vector-based computation totally eliminates the need to form any matrices, even at the element-level. This results in significant reduction of the storage cost. However, additional computations may be needed depending on the type of elements used, the number of unknowns per node and the Krylov subspace. For details, see Reference [18].

We also need to solve the non-linear rigid body dynamics equations (Equations (16) and (17)) iteratively. We start with evaluating the linear acceleration from Equation (16):

$$\mathbf{a}^{n+1} = \frac{\mathbf{F}^{n+1}}{m} - \mathbf{g} \tag{22}$$

Integrating in time the linear acceleration once, we obtain the velocity of the object, $\mathbf{v}$:

$$\mathbf{v}^{n+1} = \mathbf{v}^n + \Delta t\lfloor(\xi - 1)\mathbf{a}^{n+1} + \xi\mathbf{a}^n\rfloor \tag{23}$$

The linear displacement of the object, $\Delta\mathbf{C}$ is obtained by integrating Equation (23) in time:

$$\Delta\mathbf{C}^{n+1} = \Delta t\lfloor(\xi - 1)\mathbf{v}^{n+1} + \xi\mathbf{v}^n\rfloor \tag{24}$$

Now, we can update the position of the centre of the gravity, $\mathbf{C}$ of the object:

$$\mathbf{C}^{n+1} = \mathbf{C}^n + \Delta\mathbf{C}^{n+1} \tag{25}$$

The angular momentum equation (Equation (10)) is non-linear and needs to be solver iteratively. The non-linear iteration starts assuming that the rotation matrix $\mathbf{R}^{n+1}$ is a known matrix:

$$\mathbf{R}^{n+1} = \mathbf{R}^n \tag{26}$$

Then, at every iteration, we follow steps 1–4:

$$\text{S1: } \boldsymbol{\alpha}^{n+1} = \mathbf{R}^{n+1}\mathbf{J}_Y^{-1}\mathbf{R}^{n+1^{\mathrm{T}}}\mathbf{M} \tag{27}$$

$$\text{S2: } \boldsymbol{\omega}^{n+1} = \boldsymbol{\omega}^n + \Delta t\lfloor(\xi - 1)\boldsymbol{\alpha}^{n+1} + \xi\boldsymbol{\alpha}^n\rfloor \tag{28}$$

$$\text{S3: } \Delta\boldsymbol{\theta}^{n+1} = \Delta t\lfloor(\xi - 1)\boldsymbol{\omega}^{n+1} + \xi\boldsymbol{\omega}^n\rfloor \tag{29}$$

$$\text{S4: Form } \mathbf{R}^{n+1} \text{ from } \Delta\boldsymbol{\theta}^{n+1} \tag{30}$$

Here, $\boldsymbol{\omega}$ is the angular velocity and $\Delta\boldsymbol{\theta}$ is the angular displacement. At the end of the step 4, we check the convergence. If the convergence was not reached, we repeat steps 1–4 again otherwise we proceed with evaluating the total velocity and displacements for every computational point located on the surface of the object:

$$\mathbf{u}_P^{n+1} = \mathbf{v}^{n+1} + \boldsymbol{\omega}^{n+1} \times (\mathbf{r}_P^n - \mathbf{C}^n) \tag{31}$$

$$\mathbf{d}_P^{n+1} = \Delta\mathbf{C}^{n+1} + \Delta\boldsymbol{\theta}^{n+1} \times (\mathbf{r}_P^n - \mathbf{C}^n) \tag{32}$$

where $\mathbf{r}_P$ is the position vector for point P on the surface of the object evaluated with respect to the original co-ordinate system. $\mathbf{u}_P^{n+1}$ and $\mathbf{d}_P^{n+1}$ are the total velocity and displacement for

point P, respectively. Here these quantities are used as boundary conditions for Equations (1), (2), and (8).

5. NUMERICAL EXAMPLE

Buoyancy effect on floating object under water: Here we simulate the buoyancy effect on a rectangular object completely under water. The non-dimensional computational domain covers the volume $-0.25 \leqslant x \leqslant 4.0$, $0.0 \leqslant y \leqslant 1.25$, $-0.75 \leqslant z \leqslant 0.75$ and the object covers the volume of $1.5 \leqslant x \leqslant 2.5$, $0.35 \leqslant y \leqslant 0.65$, $-0.25 \leqslant z \leqslant 0.25$. The density of the rectangular object is half of the water. The water elevation (in y direction) is 0.75. A single cable is attached in one end to the ground at point $A(0.0, 0.0, 0.0)$ and in other end to point $B(1.5, 0.35, 0.0)$ located on the object. The density of the cable is 1.5 times the density of water. Since the cable remains completely under water, the effective density of the cable is half of the water (due to buoyancy forces). The non-dimensional Young's modulus of elasticity and the cross-section area of the cable are 1000 and 0.001, respectively.

The simulations are carried out using two finite element meshes. The coarse mesh has 199 666 nodes and 1 214 076 tetrahedral elements. The fine mesh is obtained by simply sub-dividing each element of coarse mesh into 8 elements. The cable is modelled using both Equations (8) (non-linear) and (13) (linear). Here we present 4 solutions labelled as *non-linear-coarse* for coarse mesh using Equation (8), *linear-coarse*, for coarse mesh using Equation (13), *non-linear-fine* for fine mesh using Equation (8) and *linear-fine* for fine mesh using Equation (13). For the non-linear model, the cable is discretized using 20 elements.

Initially, we assume that the cable is stress-free and completely straight connected from point A to point B. As the rectangular object rises to the free-surface of water, tensional force is generated in the cable, which causes the floating object to move toward left (x-direction) and slightly rotate counterclockwise. The simulations are carried out on the Cray T3E with 64 processors. For both meshes, the time step is 0.005 and the total of time steps is 400. In the coarse mesh simulations, the number of non-linear iterations per time step is 4 and the Krylov subspace in the GMRES is 40. In the fine mesh simulations, 5 non-linear iterations are performed at each time step and the Krylov subspace in the GMRES is set to 50.

Figure 1 shows the position of the cable at times equal to 0.5 and 1.0. In this figure, the graphs on the left and right hand sides correspond to coarse mesh and fine mesh, respectively. The difference between the solutions obtained using both meshes is small. From these graphs, we can also see that the linear and non-linear models for the cables result in almost identical solutions. However, the differences between the solutions of these two models can be seen in Figure 2. In this figure, the tensional forces for all four solutions are plotted versus time. As we can see, the difference between the linear and non-linear models can be as high as 15% in tensional forces. Also, the solutions for non-linear cable model show two pull-relax scenarios whereas the linear model experience only one. Figure 3 shows the cross-section of the solution at $z = 0.0$ at $t = 0.1$ and $t = 2.1$ (top and bottom). Here, the colour shows the water and air (light for air and dark for water) for the *non-linear-fine* solution. In this figure, we can clearly see that the water is still drifting to the tank from the top of the floating object. Our simulation model is capable of separating part of the water and remerging it. Since the set of solutions using the coarse and fine meshes for two different cases (linear and non-linear models) are very similar, we can conclude that the simulation results are reasonably accurate.

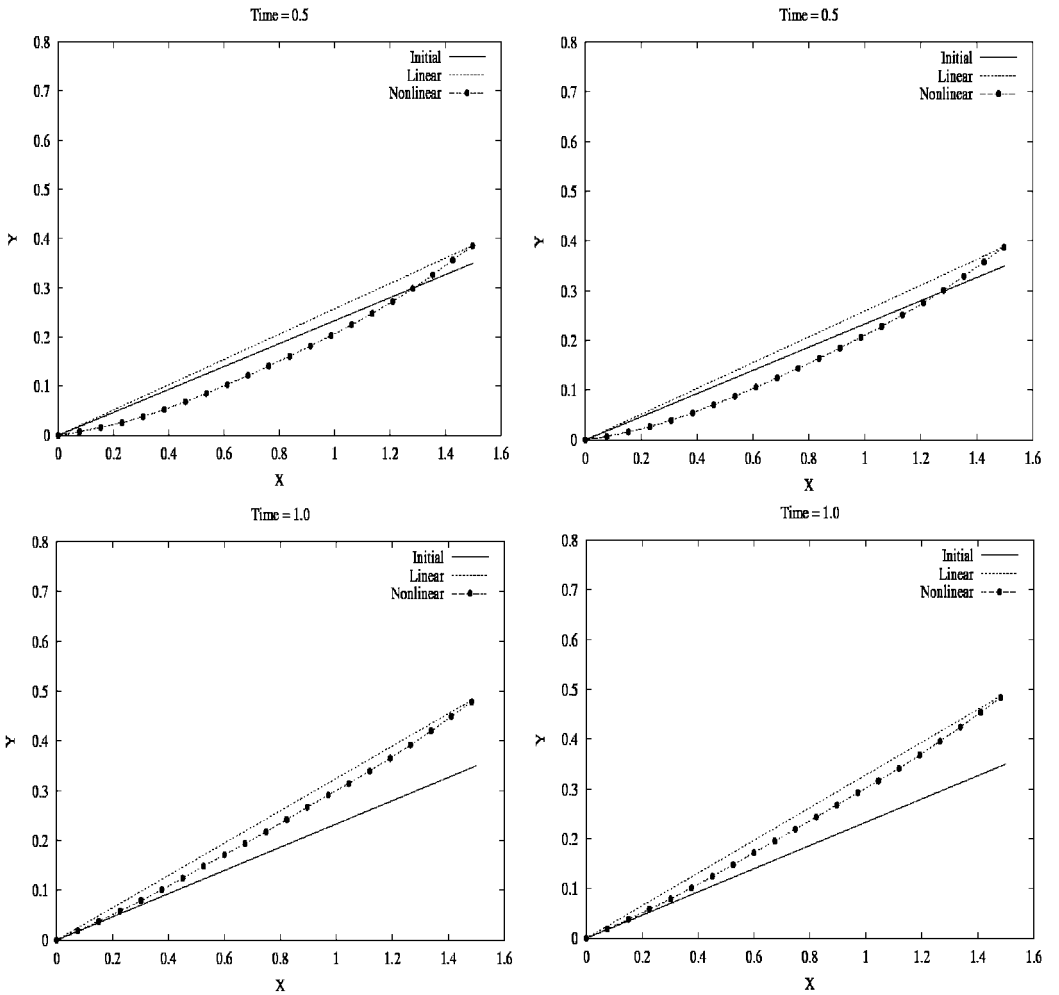

Figure 1. *Buoyancy effect on floating object under water*. The graphs show the position of the cable at time equal to 0.5 and 1.0. In this figure, the graphs on the left correspond to the solution obtained using the coarse mesh and the graphs on the right correspond to the solution obtained using the fine mesh.

Water wave impacting on a moored floating box: Here we simulate the impact of a water wave and mooring force on a floating box. To restrict the box from floating loose, we use a single hawser attached to the box and anchored to the bottom of the computational domain. The product of the hawser's modulus of elasticity and its cross section area (EA) is 500 000N/m. In this problem, a rectangular box 0.5m wide, 0.3m high, 1.0m long with density of 500 kg/m^3 (75 kg) is initially floating in a centre of a computational domain half filled with water. The computational domain is 2 m wide, 5 m long and 1.0 m high. The geometry of the computational domain, the initial position and orientation of the floating box is shown

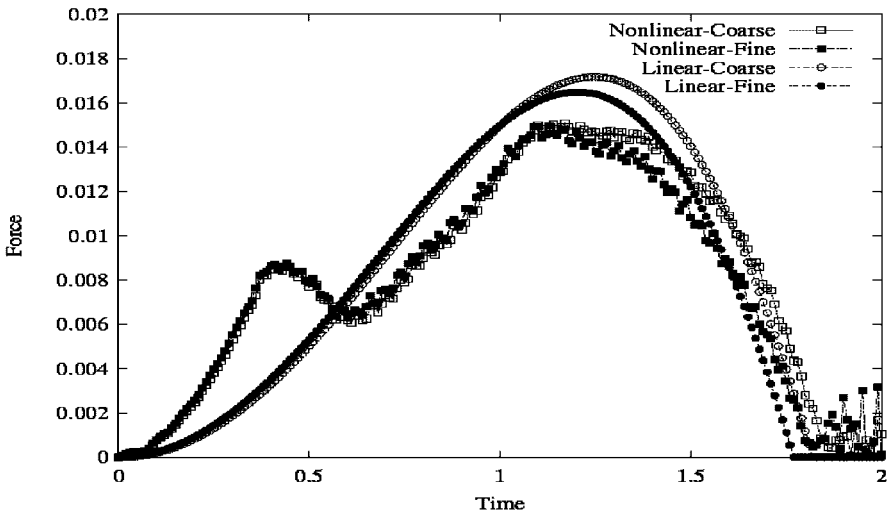

Figure 2. *Buoyancy effect on floating object under water*. The tensional forces for all four solutions versus time.

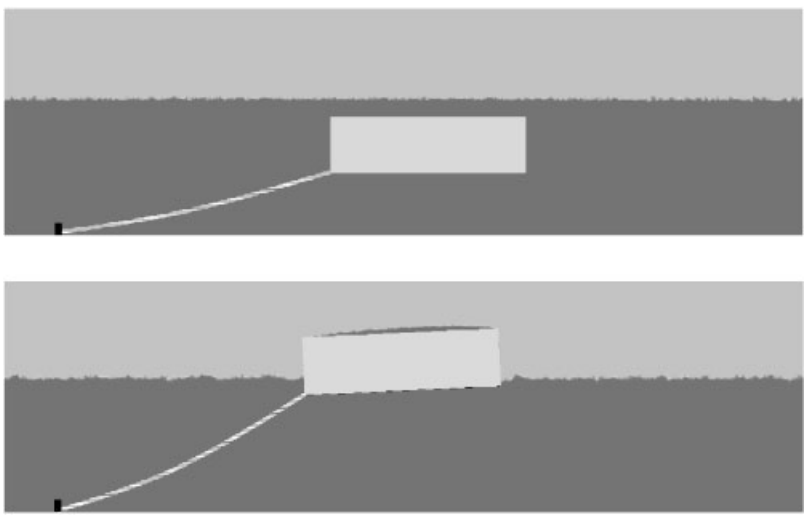

Figure 3. *Buoyancy effect on floating object under water*. Figure shows the cross section from the computational domain at $z = 0.0$ and for times at 0.1 (top) and 2.1 (bottom). Here, the tint shows the water (dark) and air (light) for the *non-linear-fine* solution.

in Figure 4. A single hawser is attached on one side to the left-bottom of the floating box and to the bottom of the computational domain on other side, as shown in Figure 4. To generate a water wave, we move the left boundary of the container with the following prescribed

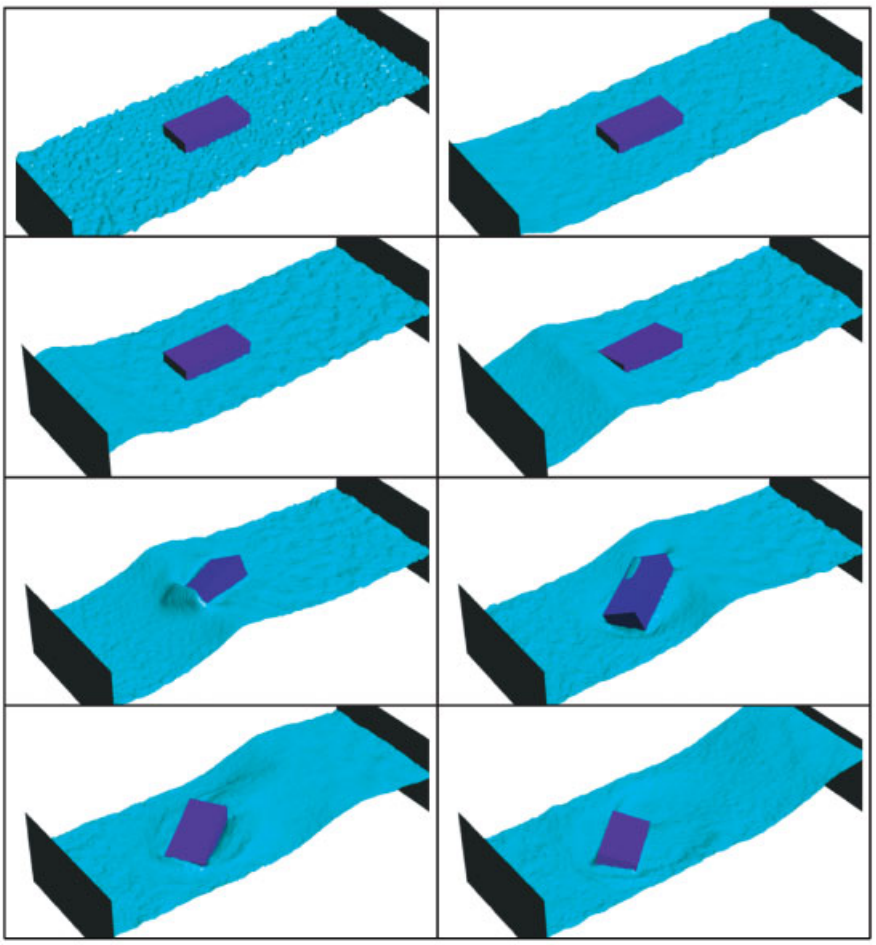

Plate 1. *Water wave impacting on a moored floating box*. The series of the frames (from left to right, top to bottom) show the time history of wave generation, two sides of the container, the free-surface of water, the position of the floating box as water wave impact on it at every 0.167 s intervals beginning at $t = 0.0$ s.

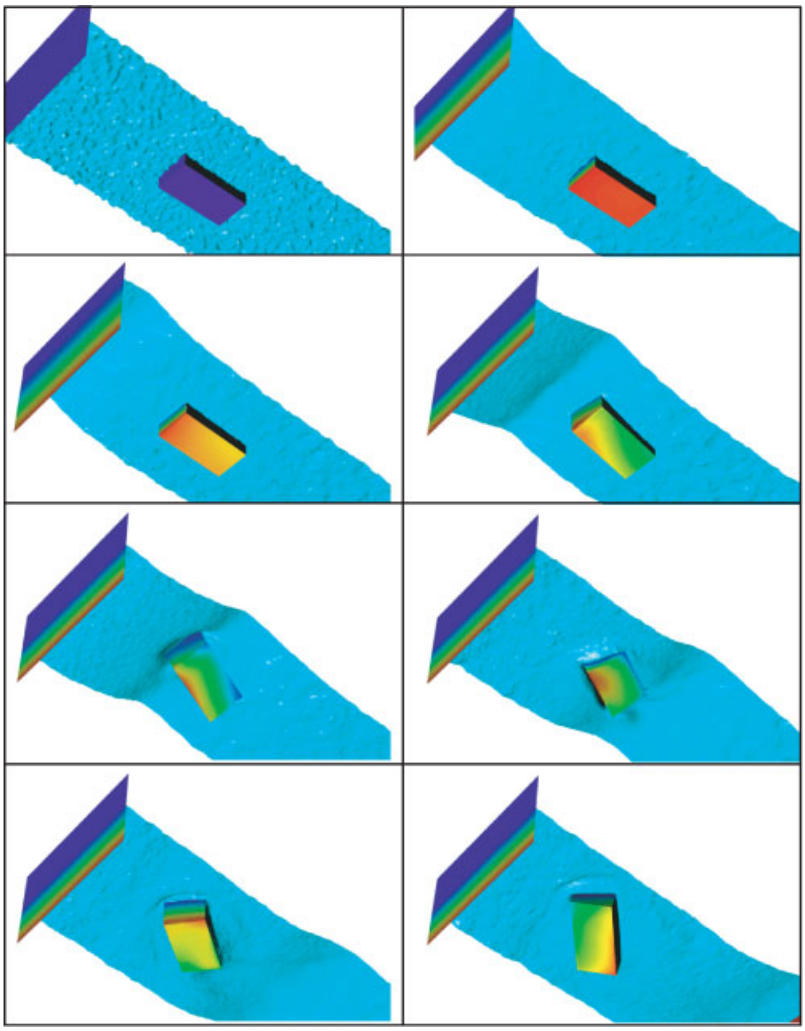

Plate 2. *Water wave impacting on a moored floating box*. The series of the frames (from left to right, top to bottom) show the time history of wave generation and wave impacting on the floating box at every 0.167 s intervals beginning at $t = 0.0$ s viewed from the bottom of the box. The colours on the box represent the pressure distribution.

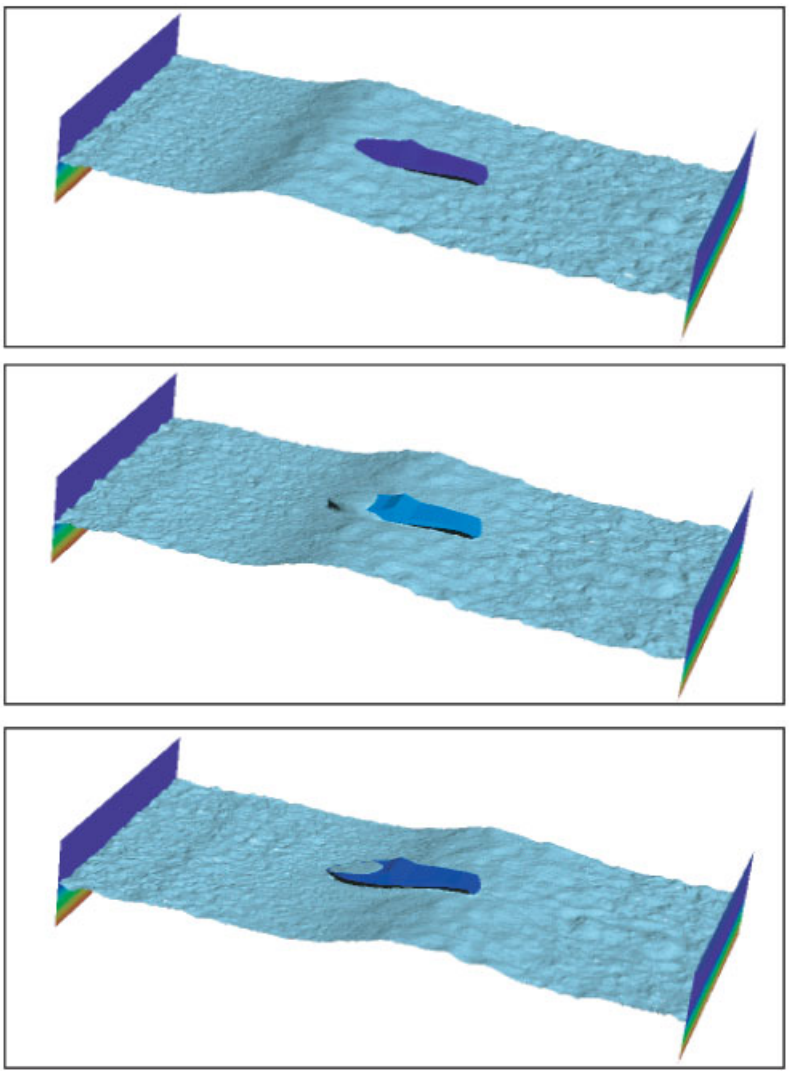

Plate 3. *Water wave impacting on moored floating model boat*. The series of the pictures show the time history of the wave generation, the position of the model boat, the free-surface of the water and two sides of the computational domain at various instances.

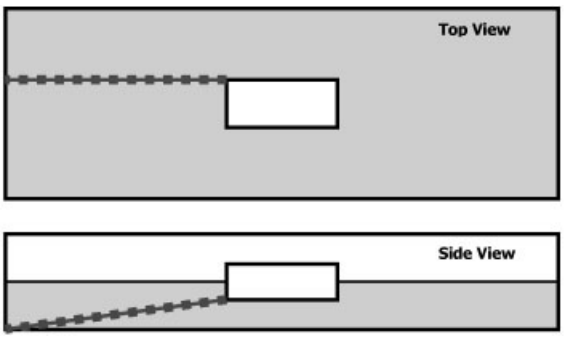

Figure 4. *Water wave impacting on a moored floating box.* The geometry of the container and the initial position and orientation of the box is shown. Also shown is a single hawser attached in one side to the left-bottom of the floating box and to the bottom of the container.

sinusoidal function:

$$x = \frac{x_{\max}}{2}\left[1 - \cos\left(\frac{2\pi t}{T}\right)\right], \quad 0 \leqslant t \leqslant \frac{T}{2} \tag{33}$$

where x is the displacement of the left boundary and $x_{\max}$ is its maximum displacement. Here T is the period and t is the elapsed time. In this simulation, $x_{\max}$ is 0.5 m and T is 1.67 s. The 3D unstructured finite element mesh consists of 87 025 nodes and 518 383 tetrahedral elements. The time step is set to 0.0167 s. The simulations are carried out on the CRAY T3E with 128 processors. The simulations are carried out for 80 time steps. Each time step takes approximately 3 min to compute.

The series of the frames in Plate 1 (from left to right, top to bottom) show the time history of wave generation, two sides of the container, the free-surface of water, and the position of the floating box as water waves impact on it at every 0.167 s intervals beginning at $t = 0.0$ s. The series of the frames in Plate 2 shows essentially the same, but viewed from the bottom. Here the colours correspond to the pressure distribution. The time history of the magnitude of the force in the cable is plotted in Figure 5. The maximum axial force in the cable is around 300 N. The time history of the vertical force exerted on the box by the water is plotted in Figure 6.

Water wave impacting on moored floating model boat: In this problem we simulate the impact of waves on a moored floating model boat. Here our model boat 0.83 m wide, 0.53 m high, 2.43 m long and weighing 200 kg is floating in a computational domain partially filled with water. The computational domain is 5 m wide, 1.5 m high and 10 m long. The moment of inertia of the model boat about the x, y, and z-axes passing through its center of gravity are 15, 75, and 70 kg-m^2, respectively. The product moments of inertia are neglected. A single cable is attached to the tip of the model boat in one end and to the bottom of the computational domain in the other end. The product of the cables' modulus of elasticity and its cross section area (EA) is 500 000 N/m. Here, we use the linear cable model. To generate a water wave, we use the same sinusoidal function in Equation (33) with the same parameters.

Two levels of finite element mesh are generated for this problem. The original unstructured mesh was created directly by our automatic mesh generator consisting of 51 320 nodes and

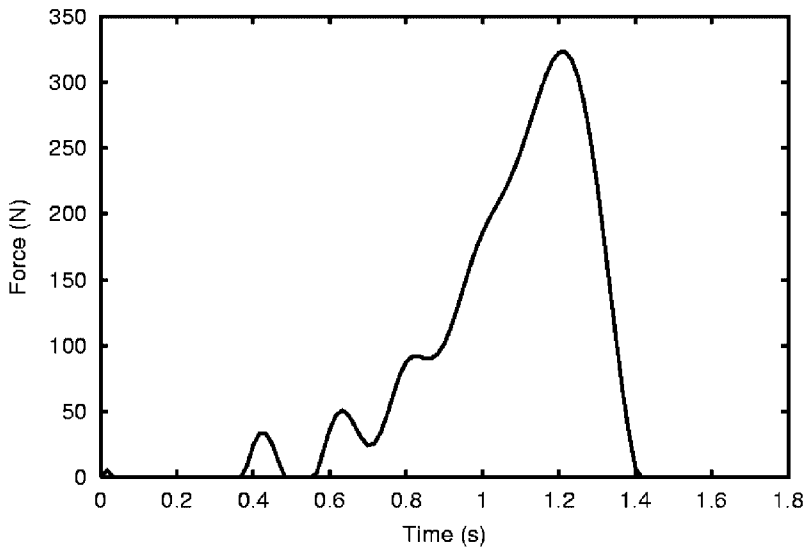

Figure 5. *Water wave impacting on a moored floating box*. Figure shows the time history of the magnitude of the force in the cable.

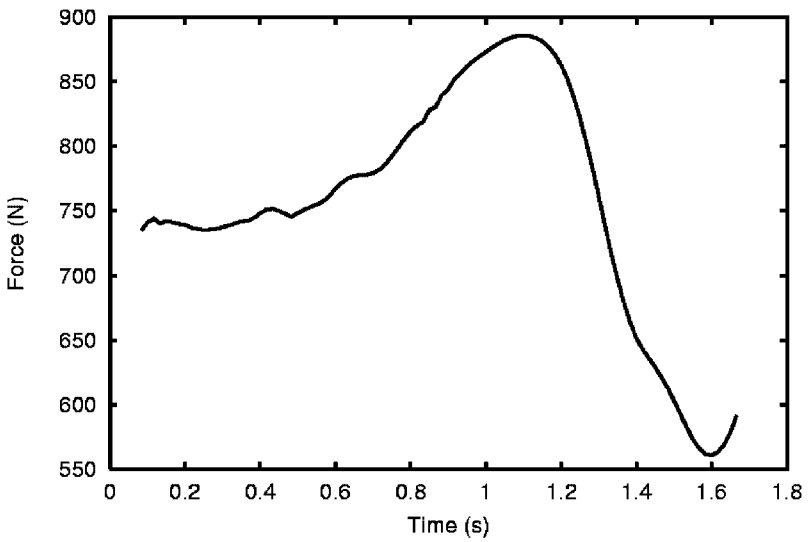

Figure 6. *Water wave impacting on a moored floating box*. Figure shows the time history of the vertical force exerted on the box by water.

299 322 tetrahedral elements. The refined mesh was then obtained by subdividing each element into 8 other elements. The computations are carried out using the refined mesh, which consists of 275 169 nodes and 2 394 576 tetrahedral elements. The numerical simulations are performed on the Cray T3E-1200 using 32 processors. At every time step we solve coupled three non-

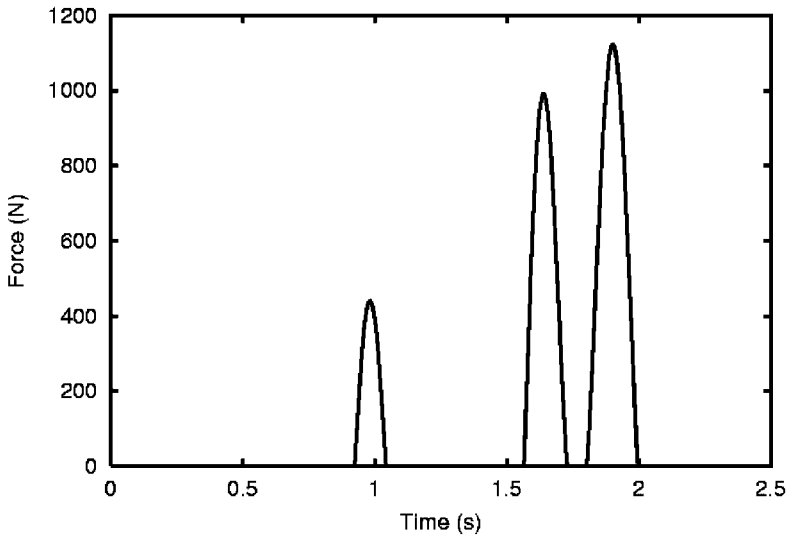

Figure 7. *Water wave impacting on moored floating model boat*. Figure shows the time history of the magnitude of the force in the cable.

linear systems of equations with 1 599 848, 1 189 346 and 410 206 unknowns corresponding to the Navier–Stokes equations, linear elasticity equations and the interface function equation, respectively.

Initially, the model boat sinks and floats frequently while preserving its original orientation. When the wave hits the boat, it creates a significant amount of drag causing the model boat to drift and as the wave passes, it generates a push. The series of pictures in Plate 3 show the time history of the wave generation, the position of the model boat, the free-surface of the water and the two sides of the computational domain at various instances. The cable experiences three disrupted tensional forces. The time history of the magnitude of the force in the cable is plotted in Figure 7. The maximum axial force in the cable is around 1150 N.

6. CONCLUDING REMARKS

We introduced a new finite element method to simulate mooring forces on floating objects. We incorporated two mathematical models for cables into this finite element method. In our approach, the cables act as constrain for the six degrees of freedom non-linear rigid body dynamic equations. Iteratively, the solutions of the Navier–Stokes equations for two incompressible fluids, the transient scalar equation governing the motion of the interface, the linear elasticity equations for mesh-moving, the linear and non-linear equations for cables and the equations motion for rigid bodies are obtained at every time step. The numerical example included 3D simulations of floating object constrained with a cable. The comparison of the solutions for linear and non-linear cables was studied. The waves impacting on moored floating object and a boat was presented.

ACKNOWLEDGEMENTS

Work funded in part by the Army High Performance Computing Research Center under the auspices of the Department of the Army, Army Research Laboratory contract number DAAD19-01-2-0014. Partial support for this publication made possible through support provided by DoD High Performance Computing Modernization Program (HPCMP), Programming Environment & Training (PET) activities through Mississippi State University under the terms of Agreement No. # GS04T01BFC0060. Views, opinions, and/or findings contained in this report are those of the author(s) and should not be construed as an official Department of the Army and Department of Defense position, policy, or decision unless so designated by other official documentation and no official endorsement should be inferred.

REFERENCES

1. Rosen BS, Laiosa JP. SPLASH nonlinear and unsteady free-surface analysis code for Grand Prix Yacht racing. *The Thirteenth Chesapeake Sailing Yacht Symposium*, Annapolis, MD, January, 1997.
2. Aliabadi S, Tezduyar T. Stabilized-finite-element/interface-capturing technique for parallel computation of unsteady flows with interfaces. *Computer Methods in Applied Mechanics and Engineering* 2000; **190**: 243–261.
3. Sundel T. *Computation of the Free-Surface Flows Around a Ship Using NS Solver FINFLO*. VTT Manufacturing Technology, 1997.
4. Aliabadi SK, Tezduyar TE. Space-time finite element computation of compressible flows involving moving boundaries and interfaces. *Computer Methods in Applied Mechanics and Engineering* 1993; **107**:209–223.
5. Hughes TJR, Hulbert GM. Space-time finite element methods for elastodynamics: formulations and error estimates. *Computer Methods in Applied Mechanics and Engineering* 1998; **66**:339–363.
6. Donea J. An arbitrary Lagrangian-Eulerian finite element method for transient fluid-structure interactions. *Computational Mechanics* 1982; **33**:689–723.
7. Farhat C, Lesoinne M, Maman N. Mixed explicit/implicit time integration of coupled aeroelastic problems: three-field formulation, geometric conservation and distributed solution. *International Journal for Numerical Methods in Fluids* 1995; **21**:807–835.
8. Johnson A, Tezduyar T. Advanced mesh generation and update methods for 3D flow simulations. *Computational Mechanics* 1999; **23**:130–143.
9. Hirt W, Nichols BD. Volume of fluid (VOF) method for the dynamics of free boundaries. *Journal of Computational Physics* 1981; **39**:201–225.
10. Sussman M, Smareka P, Osher S. A level set approach for computing incompressible two-phase flows. *Journal of Computational Physics* 1994; **114**:146–168.
11. Sethian JA. Level set method. *Cambridge Monographs on Applied and Computational Mathematics*. Cambridge University Press: Cambridge, 1996.
12. Aliabadi S, Johnson A, Zellars B, Abatan A, Berger C. Parallel simulation of flows in open channels. *Journal of Future Generation Computer Systems* 2002; **18**(5):627–637.
13. Aliabadi S, Shujaee S. Free surface flow simulations using parallel finite element method. *Simulation* 2001; **76**(5):257–262.
14. Johnson A, Aliabadi S. Application of automatic mesh generation and mesh multiplication techniques to very large scale free-surface flow simulations. *Proceeding of the 7th International Conference on Numerical Grid Generation in Computational Field Simulations*, Whistler: British Columbia, Canada, September 2000.
15. Aliabadi S, Johnson A, Abedi J, Bota K, Zellars B. Finite element simulation of hydrodynamics problems using unstructured meshes with more than one billion elements. *Proceedings of 8th International Conference on Numerical Grid Generation in Computational Field Simulations*, Honolulu, Hawaii, June 2–6, 2002.
16. Aliabadi S, Tezduyar T. Parallel fluid dynamics computations in aerospace applications. *International Journal for Numerical Methods in Fluids* 1995; **21**:783–805.
17. Hughes TJR, Brooks AN. A multi-dimensional upwind scheme with no crosswind diffusion. In *Finite Element Methods for Convection Dominated Flows*, Hughes TR. (ed.) AMD-Vol. 34, 19–35 ASME: New York, 1979.
18. Aliabadi S. Parallel finite element computations in aerospace applications. Ph.D. *Thesis*, Department of Aerospace Engineering and Mechanics, University of Minnesota, June 1994.
19. Gruttmann G, Taylor RT. Theory and finite element formulation of rubber like membrane shells using principal stretches. *International Journal for Numerical Methods in Engineering* 1992; **35**:1111–1126.
20. Saad Y, Schultz M. GMRES: generalized minimal residual algorithm for solving nonsymmetric linear systems. *SIAM Journal of Scientific and Statistical Computing* 1986; **7**:856–896.

